Emittance growth mechanisms for laser-accelerated proton beams

Andreas J. Kemp,[1,2] J. Fuchs,[1,3] Y. Sentoku,[1] V. Sotnikov,[1] M. Bakeman,[1] P. Antici,[1,3] and T. E. Cowan[1]
[1]*Physics Department, University of Nevada, Reno, Nevada 89557, USA*
[2]*Lawrence Livermore National Laboratory, Livermore, California 94551, USA*
[3]*Laboratoire pour l'Utilisation des Lasers Intenses, UMR 7605 CNRS-CEA-École Polytechnique-Université Paris VI, Palaiseau, France*

(Received 28 January 2006; revised manuscript received 5 January 2007; published 3 May 2007)

In recent experiments the transverse normalized rms emittance of laser-accelerated MeV ion beams was found to be <0.002 mm mrad, which is at least 100 times smaller than the emittance of thermal ion sources used in accelerators [T. E. Cowan *et al.*, Phys. Rev. Lett. **92**, 204801 (2004)]. We investigate the origin for the low emittance of laser-accelerated proton beams by studying several candidates for emittance-growth mechanisms. As our main tools, we use analytical models and one- and two-dimensional particle-in-cell simulations that have been modified to include binary collisions between particles. We find that the dominant source of emittance is filamentation of the laser-generated hot electron jets that drive the ion acceleration. Cold electron-ion collisions that occur before ions are accelerated contribute less than ten percent of the final emittance. Our results are in qualitative agreement with the experiment, for which we present a refined analysis relating emittance to temperature, a better representative of the fundamental beam physics.

DOI: 10.1103/PhysRevE.75.056401 PACS number(s): 52.38.Kd, 29.27.Fh, 52.40.Kh, 52.70.Nc

I. INTRODUCTION

Research on particle acceleration with ultrashort intense laser pulses ($\tau_L < 1$ ps; $I\lambda^2 > 10^{18}$ W/cm^2 μm^2) has gained significant momentum for both electron beams accelerated in dilute gas jets [1] and ion beams that are accelerated in the quasineutral expansion of thin laser-irradiated solid foils [2]. Distinct features of such laser-accelerated ion beams are maximum particle energies of up to 60 MeV for protons and an excellent beam quality [3], i.e., rapid generation and low transverse divergence, as well as extremely low emittance, on which we want to focus here. Beam emittance is defined as correlation between the particles' transverse position relative to the beam center and their transverse velocity, normalized to their longitudinal velocity [4]. An ideal beam with a direct correlation is said to have zero transverse emittance. Note that low beam emittance is distinct from a diverging or converging beam, which is a separate issue that has been studied elsewhere [5]; a low-emittance beam is laminar, independent of its divergence. Ion beams accelerated from targets that are not specially prepared have a natural large energy spread in the longitudinal direction [6]. This issue will not be addressed here, either. In a recent experiment, the transverse proton root-mean-square (rms) emittance for particle energies >10 MeV has been determined to be smaller than 0.004 mm mrad [3]. This is more than 100 times better than the emittance of current ion accelerator beams. At the same time, the micrometer-scale acceleration length potentially allows for highly compact accelerator structures. These properties make laser-driven proton accelerators attractive for various applications, ranging from inertial confinement fusion to cancer therapy [7–11].

In this paper we investigate the theoretical background of transverse emittance growth mechanisms for fast, laser-accelerated ion beams. Our task is to elucidate the physical origins of the emittance of laser-accelerated ion beams under idealized conditions. This is done by using analytical estimates on the one hand, and numerical simulations for the subpicosecond dynamics of the target during and shortly after the laser interaction on the other hand. The centerpiece of this article are highly resolved particle-in-cell simulations that include a Monte Carlo description of Coulomb collisions and resolve the filamentation of the laser-generated electron jets which turn out to be mainly responsible for the ion beam emittance. We also present a refined analysis of the experimental results presented in Ref. [3] that yields a lower limiting value for the proton beam emittance and express the transverse beam quality in terms of a temperature. The latter is independent of the source size, so that a comparison with our simulation is possible [12]. We conclude by discussing the role of numerical effects.

General assumptions

In order to simplify the analysis of the sources of emittance growth we have made a number of assumptions the validity of which we will discuss in the following.

Considering the ion beam as composed out of a large number of individual beamlets that start from different positions on the rear surface of the laser-irradiated foil, the transverse beam emittance can be defined by the correlation between the initial beamlet position and its angle relative to the target normal, as pointed out above. Any deviation from this ideal inevitably leads to an overlap of individual beamlets downstream. On the one hand, this overlap can be caused by a corrugated target surface where the local target normal points in different directions for "neighboring" beamlets. Intentionally corrugating the target surface has been used to determine the absolute source size of the proton beam [3]. Here we want to exclude this scenario and consider only uniform targets. We also ignore intensity fluctuations in the laser spot or other imperfections. What remains is a transverse beam structure that is related to modulations in the electron beam due to filamentation, or to the finite size of the

laser spot. On the other hand, the overlap of neighboring beamlets can be caused by thermal effects, i.e., collisions between electrons and ions near the target surface; this will cause a finite beam emittance even within a single beamlet. The task of this paper is to clearly separate these phenomena and to identify the mechanism that is responsible for the measured ion beam emittance.

For the sake of simplicity we will assume that all accelerated ions originate from the rear target surface. Recent experiments comparing front and rear surface acceleration mechanisms under various conditions have found that a small fraction of ions is accelerated at the front of the target [13]. These ions have not only smaller energies than those accelerated off the back of the foil, they also have larger transverse and longitudinal emittance since they have passed through the solid target at relatively low speed and undergone many collisions or possibly beam instabilities inside the target. This will not be considered here. Furthermore, experimental evidence suggests that the imaging quality of the ion beam depends on the material properties of the target [14]. While conductor targets, i.e., metals, give high quality proton beams resulting in smooth angular distributions, those from insulator targets are smeared out. This is indicative of spatially nonuniform ion acceleration, which can be explained by (a) poor electron transport caused by ionization [15] or (b) the difference in resistivity between target materials. While we will discuss the effect of the target resistivity on the transverse uniformity of the beam, we will ignore nonuniformities due to ionization, and therefore restrict our analysis to metal targets.

Multispecies effects can lead to a disruption of flow laminarity in both longitudinal and transverse direction at low ion energies [16]. Experimental results, however, show that the outer layer on target surfaces is typically covered by hydrocarbons, so that one always deals with multiple charge state ions at low ion energies. In order to neglect such effects we will focus on high-energy protons at energies >1 MeV/u.

For a spatially uniform electron current through an ideal conductor target, the only mechanisms that can lead to thermal emittance in a beam lifting off from a solid target are collisional energy coupling before and during acceleration, and noncollisional energy transfer via beam instabilities. We demonstrate that the emittance of the accelerated ion beam is limited by the filamentation of the electron beam in the bulk target in combination with collisional effects. Alternative physical origins of beam emittance are investigated and found to be of minor importance. Recombination of electrons and ions in the expanding plasma is not considered in this work. At the moment there is only little experimental evidence for a small number of neutrals found in experiments [17], but no relative numbers are available.

II. EXPERIMENT

Experimentally, the first attempts to measure the beam emittance or source size have been made by using projection, on a far distant film, of objects like knife edge [18] or meshes [19] placed in the ion beam path. The transverse emittance was estimated to be <0.5 mm mrad [18]. However, the ion beam does not propagate ballistically close to the target and passage of the beam on the object induces charge-up that deflects the beam. Therefore, the beam emittance or source size cannot be reconstructed precisely from such measurements. To overcome these limitations, we have used a new technique that allows us to directly image the initial accelerating sheath and to fully reconstruct the transverse phase space. This is done by producing fiducials of the beam flow. Such fiducials are produced by purposefully micromachining shallow grooves on the nonirradiated rear target surface. Doing this produces a periodic modulation of the beam angular envelope [3,20] as shown in Fig. 1(a). Indeed, as protons are first accelerated normal to the surface by the strong electrostatic field induced by the dense relativistic electron sheath, the grooves on the surface induce a modulation of the takeoff angle. Due to the global sheath expansion, an overall near-linear divergence is added to this initially imprinted angular modulation of the beam. Projected on a film stack far away, this results in a modulation of the proton dose. Using such modulations of the beam intensity, as we can directly measure on the film the position at which protons were emitted from the target rear surface and the angle at which they have been emitted, we can thus reconstruct the transverse phase space $(x,x'=p_x/p_z)$, where x is the transverse dimension, z the longitudinal dimension, and x' is the particles' divergence. The root-mean-square (rms) value of the normalized emittance ε_N, at a specific beam energy, is then determined as $\varepsilon_N = (|p|/mc)[\langle x^2\rangle\langle x'^2\rangle - \langle xx'\rangle^2]^{1/2}$, where m is the ion mass, and c is the velocity of light. It is proportional to the volume of the bounding ellipsoid of the distribution of particles in

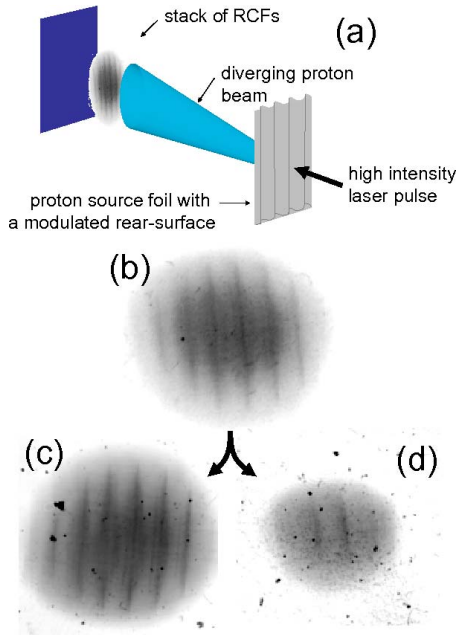

FIG. 1. (Color online) Experimental determination of proton beam emittance. (a) Schematic representation. Angular distributions on RCF of protons accelerated from an 18 μm thick Al flat target irradiated at 10^{19} W/cm^2 as observed on (b) the unseparated MD55 dosimetry film [corresponding to Fig. 2(c) of Ref. [3]] and (c), (d) the two separated layers that compose the film in (b).

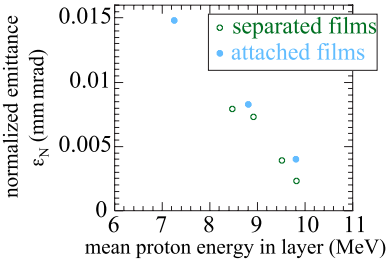

FIG. 2. (Color online) Normalized rms emittance inferred from the unseparated and separated films shown in Figs. 2(a)–2(c) of Ref. [3] as a function of the mean proton energy in each layer or film.

transverse phase space. For the film shown in Fig. 1, we have used the 30 TW Trident laser at the Los Alamos National Laboratory. Laser pulses of 20–30 J, 850 fs full width at half maximum duration, and 1 μm wavelength were focused at an irradiance of 10^{19} W/cm^2 at normal incidence onto the front surface of 18 μm thick Al foils. On the rear surface of these foils we micromachined shallow grooves, 200 nm deep spaced 3.6 μm apart. The accelerated protons were detected in multiple layers of radiochromic film (RCF) densitometry media placed 68 mm from the target. The spatial distribution of the protons in a given RCF layer gives the angular emission pattern at a specific interval of proton energy, as shown in Fig. 1(a). As the specific RCF used in this experiment is comprised of two sensitive layers sandwiched together, and is therefore sensitive to protons of different energies, we can access to a more precise measurement of the emittance by separating these two sensitive layers which compose the films. Indeed, as we have observed that the beam emittance was varying with the energy of the protons [3], analyzing the whole film gives only a result averaged over the two proton energy range that corresponds to the two layers. The two sensitive layers of each film are 16 μm thick and separated by 75 μm of adhesive and polyester. The layers were separated using a bath of acetone and ethyl alcohol. The films were placed in acetone for approximately two days in an airtight container until they were easily split into two halves. The center piece of polyester was removed from the half of the film on which it was still affixed. Both halves now free of all Mylar were placed in ethyl alcohol for approximately 1 day in an airtight container. The halves were removed from the ethyl alcohol for 10 min until all the alcohol had evaporated off and the films had turned clear, at which point they were scanned. An example of the outcome of such separation is shown in Fig. 1. Since this chemical process affected the color and the optical density of the separated layers, we had to recalibrate the modified layers with reference to the calibrated, unseparated film in order to get a correct proton number on each of the separated layers. This was made by building a calibration curve between the added optical densities of the separated layers and the optical density of the unseparated film, the absolute dose calibration of which is known [21,22]. Then the transverse phase space plot of the proton beam and hence the emittance [3] could be estimated for the different separated layers and compared to the one for the unseparated films, as shown in Fig. 2. For protons of up to 10 MeV, the transverse emittance is as low as 0.0025 mm mrad, i.e., more than 100-fold better than typical RCF accelerators and at a substantially higher ion current (kA range). This is equivalent to saying that the beam is originating from an extremely small virtual source, i.e., positioned in front of the target. We have deduced from this technique that the source size was ≈ 4 μm for the highest energy protons. It is important to note that this value is actually an upper limit that is limited by the experimental technique of producing the fiducials in the beam flow and that the real emittance could be even lower. The emittances retrieved from the separated layers are slightly lower than the ones measured from the unseparated films. This is mainly due to a lesser angular width of the beamlets arising from the surface modulations as the energy bin of the separated films are smaller. Note that the values presented in Fig. 2 are still upper limits on physical emittance, as described in detail in Ref. [3].

By measuring the angular width of the sharp cusps in the proton angular distribution we can also determine the proton beam temperature directly, which is easier to compare between experiments and with our simulations below. The angular width of the cusps is the standard deviation of the spatial groove width, divided by the distance between the target and the RCF film stack. The angle of a proton accelerated in z direction to a total velocity $v \approx v_z$ with transverse velocity v_x is $\theta_x = v_x/v$, so the standard deviation is $\sigma_{v_x} = v\sigma_{\theta_x} = (kT/m_p)^{1/2}$; hence

$$kT = m_p v^2 \sigma_{\theta x}^2 = 2E_p \sigma_{\theta_x}^2. \quad (1)$$

The result of this analysis for a set of four temperatures is shown in Fig. 8 and will be discussed in Sec. 4(b) below.

III. SCENARIOS FOR EMITTANCE GROWTH

In general the mechanism for the acceleration of protons off the rear surface of intense, short pulse-laser irradiated targets is well understood [2,23,24]. Before the main pulse, a nanosecond prepulse generates several microns of preplasma in front of the target. As the intense femtosecond pulse interacts with this preplasma, a large number of electrons is accelerated into the bulk target. When these electrons pass through the target they generate a strong electrostatic field on the rear surface which then ionizes a thin sheath of ions and accelerates them. These ions come from a thin layer of hydrocarbons that covers most targets in realistic experiments, which is easily field-ionized and provides mostly protons, which have the highest charge-to-mass ratio, and various charge states of carbon and oxygen.

The time history of the ion acceleration process off a laser-irradiated foil target can be roughly divided into two stages: (1) Before substantial ion motion sets in; (2) The expansion stage, which begins when the density of the accelerated ions has dropped to roughly 1/3 of its initial value. In between the two there is a complex intermediate stage (3) which we will describe by a detailed computer simulation in Sec. IV below. For the first two stages we want to give naive estimates of how and how much emittance will be generated.

The duration of stage (1) which ions spend in the dense plasma can be estimated from a simple dimensional analysis

$$\delta t \approx \sqrt{\frac{m_p \lambda_D}{eE_0}} \quad \text{with } E_0 = (4\pi n_e k_B T_e)^{1/2}, \tag{2}$$

where m_p is the proton mass and E_0 stands for the electric field behind the target. It is calculated from the hot electron density n_e and temperature T_e [23]. For an MeV population of electrons at critical density 10^{21} cm^{-3} we find $\delta t \approx 20$ fs. One also needs to be aware of the fact that deeper ion layers will be accelerated later than the outmost layer. The thickness of the proton layer on the rear surface of foil targets has been measured to be roughly 20 Å [25], i.e., thin compared to both the skin length on which the electric field can penetrate the target and the Debye length of the hot electrons.

In the following we will consider collisional and kinetic effects separately in stages (1) and (2). In Sec. IV we present an integrated model with both effects for the intermediate stage.

A. Electron-ion collisions near the target surface

Before ions are accelerated by the electrostatic field behind the target, their heating can be described by rate equations for electron and ion temperatures. This simple approach assumes a spatially uniform situation—effects of nonuniformity and expansion will be taken into account in Sec. IV below. The conclusion from this simple model approach is that hot electrons, due to their large temperatures, couple only slowly to ions. Therefore, the cold electron population plays a central role in transferring energy from the hot electrons to the ions. The rate equations are

$$\frac{dT_i}{dt} = \nu_\epsilon^{ic}(T_c - T_i) + \nu_\epsilon^{ih}(T_h - T_i),$$

$$\frac{dT_h}{dt} = \nu_\epsilon^{hi}(T_i - T_h) + \nu_\epsilon^{hc}(T_c - T_h),$$

$$\frac{dT_c}{dt} = \nu_\epsilon^{ci}(T_i - T_c) + \nu_\epsilon^{ch}(T_h - T_c). \tag{3}$$

Under "ideal plasma" conditions the energy transfer between charged particle species α and β occurs at a rate [26]

$$\nu_\epsilon^{\alpha\beta} = \frac{8\sqrt{2\pi}e^4}{3} \frac{(m_\alpha m_\beta)^{1/2} Z_\alpha^2 Z_\beta^2 n_\beta \ln \Lambda}{(m_\alpha k T_\beta + m_\beta k T_\alpha)^{3/2}}, \tag{4}$$

where masses and density are given in cgs units and $\ln \Lambda$ is the Coulomb logarithm, which depends only weakly on plasma conditions [26]. For our numerical estimates, as well as in our computer simulations described in Sec. IV, we use $\ln \Lambda = 5$. Equation (4) assumes that each individual species is in thermal equilibrium, i.e., has a Maxwellian distribution function. The rate at which this equilibrium is established for single species α can be estimated by $\nu_\epsilon^{\alpha\alpha}$. Under the conditions relevant for the experiment, i.e., with a cold electron temperature $T_c = 50$ eV at solid density, this rate corresponds to a time of roughly 0.1 fs, and several femtoseconds for protons.

Since recent experiments provide only time-integrated information about the cold electron temperature T_c at the rear target surface, we have to speculate about T_c before and during ion acceleration. As a rule of thumb, it has been found experimentally that the background temperature in the target is 1–2 eV per joule of laser energy [27]. At an estimated laser pulse energy of 20–30 J, as reported in the experiment described in Sec. II, we arrive at $T_c \approx 50$ eV.

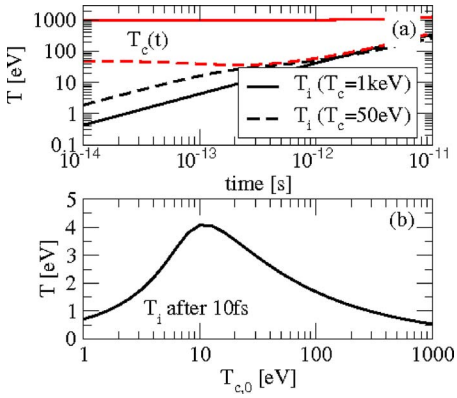

FIG. 3. (Color online) (a) Temporal history of the ion (black) and electron (gray) temperatures as found from rate equations (3) in two cases: $T_{c,0} = 50$ eV (full lines) and $T_{c,0} = 1$ keV (broken lines). (b) Dependence of ion temperature at time 10 fs on the initial conditions for cold electron temperature. All with $n_e = 4 \times 10^{22}$ cm^{-3}, $T_h = 1$ MeV, and $Z = 1$.

In theory, the initial value of the cold electron temperature $T_c(0)$ is set by several factors, including hydrodynamics of the ASE laser prepulse, i.e., possibly shock waves and radiation from the laser interaction, and by ionization dynamics on a subpicosecond time scale that is followed by ohmic heating due to a resistive return current to relativistic electron jets driven into the solid by the laser interaction. As an example, let us estimate the temperature of such a return current in an aluminum target with a relativistic current $j_{\text{hot}} \approx n_c c$, where $n_c = 10^{21}$ cm^{-3} is the critical density at which the laser is absorbed. The cold return current is carried by an electron density $n_{\text{ret}} = 2 \times 10^{23}$ cm^{-3}, so that the resulting velocity is $v_c \approx 0.01c$, corresponding to a temperature of roughly 50 eV.

Figure 3 shows thermal equilibration between electrons and ions as described by Eqs. (3) for two relevant cases. The initial value of the hot electron temperature is 1 MeV and their density is set to 10^{21} cm^{-3} which is the critical density for laser light at a wavelength of 1 μm. These parameters correspond to the interaction of a 10^{19} W/cm^2 intensity laser pulse with a solid target as specified in the simulation; see Sec. IV. In the first case the cold electron temperature is initialized with 50 eV as discussed above, while in the second case it is initially 1 keV. We use this latter value for the bulk plasma temperature to avoid numerical heating in the numerical simulation in Sec. IV. Figure 3(a) shows the time history of cold electron and ion temperature for the two cases mentioned above. It is interesting to note that after 10 ps ions and electrons will have equilibrated for all values of $T_c(0)$, as long as hot electrons are present. Figure 3(b) shows the dependence of the ion temperature at 10 fs on the initial value of the cold electron temperature $T_c(0)$. Since the ion acceleration dynamics itself is almost independent of that param-

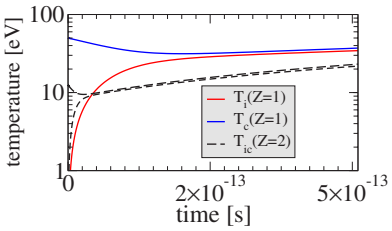

FIG. 4. (Color online) (a) Temporal history of the ion (black) and cold electron (gray) temperatures as found from rate equations (3) in two cases, for $Z=1$ with $T_{c,0}=50$ eV (full lines) and for $Z=2$ with $T_{c,0}=12.5$ eV (broken lines).

eter, it is interesting to see how our choice of the cold plasma background affects the ion temperature at a given instant in time. As Fig. 3(b) shows, the ion temperature is relatively insensitive to the choice of $T_c(0)$. Note that the heating time scale between the hot electrons and the ions alone is several microseconds. This means that the ion temperature at 10 fs is not sensitive to the initial hot electron temperature. Our choice of 10 fs as the time at which we compare temperatures is motivated as the time during which ions travel over the 20 Å when exposed to the maximum longitudinal electric field behind the target.

The presence of higher-charge state ions can be included by introducing additional equations to system (3). However, the effect of high charge-state ions on their final temperature is much smaller than expected from direct coupling, i.e., when using only a single electron species. The reason is that Eqs. (3) are dominated by two largely different rates: The energy exchange rate between hot and cold electrons, and that between electrons and the highest ion charge state. Energy exchange in between different ion species is always much faster than that between ions and electrons. In an environment where $T_h \gg T_c$, the coupling between hot- and cold electrons is much slower than that between cold electrons and ions. This effect is illustrated in Fig. 4 showing the two time scales that are related to electron-electron and electron-ion coupling for our "standard" case described above and the case $Z=2$ with a reduced value of $T_c(0)$.

Following our earlier argument, the larger number of electrons available for the return current leads to a drop in the cold electron temperature proportional to Z^2. Therefore, the equilibration between cold electrons and ions is faster, but it leads to smaller ion temperatures on extremely short time scales: sub-fs for $Z=4$, compared to $\nu_\epsilon^{pc}=(500\ \text{fs})^{-1}$ for the proton "reference" case. The exchange between hot and cold electrons occurs on a much longer time scale defined only by the hot electron density and temperature (which are assumed to be independent of the target Z). In the limit of high-Z the ion temperature at a fixed time relevant for the ion liftoff (tens of fs) remains therefore almost constant. Let us discuss three alternatives with respect to the initial values of the cold electron density and temperature. (A) Our "reference" case from Fig. 3 is defined by $Z=1$, $n_c=n_i=4\times10^{22}$ cm^{-3}, and $T_c(0)=50$ eV. The resulting ion temperature at 10 fs is 2 eV. (B) With $Z=4$ the cold electron density is $n_c=Zn_i$ and $T_c(0)=50/Z^2$ eV. This results in an ion temperature of ≈3 eV at 10 fs. (C) Assume that there is a small amount of protons while the dominant charge state is $Z=4$ and the number of hot electrons is consistent with that value. The result in this case is similar to case (A). Note that this naive model can only represent a guidance on the ion heating process. The assumptions that are required to validate the results for higher charge states have to be checked by more detailed computer simulations.

B. Kinetic effects near the target surface

When considering collisionless energy transfer between electrons and ions near the target surface we can distinguish between one- and multidimensional effects. The latter will be considered explicitly in Sec. IV C below; we will show that multidimensional effects are responsible for about 90% of the measured emittance. Their dependence on the collisionality in the bulk target, and possibly ionization effects, are likely responsible for the low-quality shots mentioned in Ref. [14], in that these effects degrade the uniformity of electron transport through the target already at the laser interaction region. However, for the remainder of Sec. III we will assume uniform electron transport. One-dimensional instabilities like Langmuir turbulence can transfer energy from the hot electron population into the cold background, thereby setting the pace at which ions are heated—see Fig. 3. To study the effect of kinetic energy transfer between electrons and ions, we have compared the collisional simulation presented below with a well-resolved, collisionless fiducial run. Since the latter shows no significant ion heating, apart from numerical effects (see Sec. IV D), we conclude that longitudinal instabilities in the dense plasma play no role in ion heating.

C. Collisional effects in the expanding plasma

In the late expansion stage, which sets in after the ion density of the beam has dropped substantially, collisional energy transfer between electrons and ions can still be described by the rate equations (3), only now using a time history for the electron and ion temperature and density. The latter can be included as a self-similar expansion model [23]. In the typical case where the laser pulse length $t_L\approx1$ ps, it is reasonable to assume that the expansion is isothermal during the laser interaction time, i.e., the electron temperature is constant, and becomes adiabatic as soon as the laser pulse is off. Then the electron temperature evolves with time as

$$T_e = T_{e0}[1+(\Omega t)^2]^{-1} \tag{5}$$

with a time constant $\Omega\approx1$ ps^{-1}, while being spatially uniform. At the same time ion and electron densities drop exponentially due to debunching, i.e., the longitudinal stretch of the beam, and the natural beam divergence that comes with the thermal energy of the beam. Using profiles of density with time and space together with a constant temperature of the electrons, one can now deduce a lower limit for the ion thermal emittance due to collisions in the beam for (i) the isothermal solution and (ii) an adiabatic solution. Integrating Eqs. (3) with these histories yields an upper limit for the ion thermal emittance that can be caused by electron-ion colli-

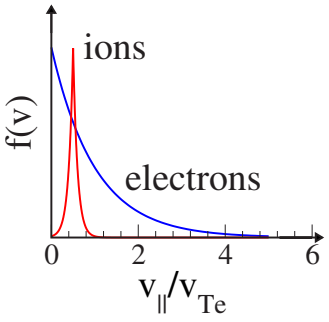

FIG. 5. (Color online) Schematic representation of the potentially unstable combination of a quasimonoenergetic beam on a thermal background. The instability threshold is given in Eq. (9).

sions in the expanding plasma. For its value we find 0.05 eV; the reason behind this small value is the exponential drop of the density, while temperature drops as a power law. As a consequence the energy transfer rate drops exponentially with time.

D. Kinetic effects in the expanding plasma

The combination of a uniform locally monoenergetic charged particle beam in a background of thermal electrons, shown schematically in Fig. 5, is potentially unstable [28]. An ion beam has negative-energy modes if its relative velocity exceeds a certain fraction of the background thermal velocity, as will be discussed below. These modes can lead to a collisionless widening of the beam distribution in both transverse and longitudinal direction, i.e., they generate emittance. For reasons of simplicity, our present analysis is limited to longitudinal ion-acoustic modes. One can, however, extend the argument to transverse modes in that the latter will be growing slower than the longitudinal one. Our analysis therefore represents an upper limit of the growth of ion acoustic modes in the expanding plasma, and the fact that longitudinal modes do not occur can be extended to transverse modes. To quantify the role of negative-energy modes in a quasineutral plasma expansion, we compare their growth lengths to the gradient length in the expanding flow, using an analytic self-similar model [23]. As a result, we find that instabilities can only occur at late times in terms of the beam acceleration, or far behind the beam expansion front. They will most likely not affect the most energetic ions that are measured in an experiment [3]. We restrict our analysis to modes parallel to the beam, which are expected to grow faster than the modes transverse to the beam expansion. We also restrict our analysis to proton beams, while it can be easily expanded to arbitrary ions. Our results serve as an upper limit for the actual transverse spread in momentum space of the proton beam, i.e., its emittance in a real experiment.

The dispersion relation of an ion beam with velocity v_b in the background of thermal electrons is given by [28]

$$1 + \frac{1}{k^2\lambda_D{}^2}\left(1 + \imath\sqrt{\frac{\pi}{2}}\frac{\omega}{kv_{Te}}\right) - \frac{\omega_b^2}{(\omega - k_\parallel v_b)^2} = 0, \tag{6}$$

where λ_D is the background electron Debye length, $k_\parallel$ is the wave vector parallel to the beam, and $\omega_b = (4\pi n_b e^2/m_b)^{1/2}$ is the proton beam plasma frequency. The beam particles have mass m_b; their density $n_b = n_e$ is assumed to be equal to the electron density so that the plasma is quasineutral.

The solution of the dispersion relation gives the oscillations and growth rate of unstable modes as

$$\omega(k) = k_\parallel v_b - \omega_b \frac{k\lambda_D}{(1 + k^2\lambda_D{}^2)^{1/2}}, \tag{7}$$

$$\gamma(k) = \sqrt{\frac{\pi}{8}}\omega\frac{\omega_b}{\omega_p(1 + k^2\lambda_D{}^2)^{3/2}}, \tag{8}$$

where $\omega_p = (4\pi n_e e^2/m_e)^{1/2}$ is the electron plasma frequency. The threshold for the onset of the instability parallel to the beam is

$$v_b \geqslant \frac{\omega_b}{\omega_p} v_{Te}. \tag{9}$$

Inserting Eq. (7) into Eq. (8), we can calculate the growth rate of the ion-acoustic instability for the fastest-growing mode $k \approx \lambda_D{}^{-1}$

$$\gamma = \frac{\sqrt{\pi}}{8}\omega_b\frac{\omega_b}{\omega_p}\left[\frac{\omega_p}{\omega_b}\frac{v_b}{v_{Te}} - \frac{1}{\sqrt{2}}\right], \tag{10}$$

while assuming a uniform beam and background plasma. The growth length L_γ over which this instability develops is given by the ratio of the rate γ and the local group velocity

$$v_g \equiv \frac{d\omega}{dk} = v_b - \frac{\omega_b\lambda_D}{(1 + k^2\lambda_D{}^2)}. \tag{11}$$

For the mode $k = \lambda_D{}^{-1}$ we find

$$L_\gamma = \frac{8}{\sqrt{\pi}}\frac{\omega_p}{\omega_b}\lambda_D. \tag{12}$$

In the case of a uniform proton beam, this yields $L_\gamma \approx 200\lambda_D$. Now we account for the nonuniform density in the expanding plasma, using the classical self-similar plasma expansion model under isothermal conditions [23]. Note that the ion density predicted by this model drops exponentially behind that target. To study the growth of negative-energy modes in this environment, we compare L_γ to the local density gradient length. The latter is given by $L_\Delta = c_s t$, where c_s is the ion sound velocity $c_s = \sqrt{kT_e/m_b}$. An instability has a chance to grow if

$$L_\gamma \leqslant L_\Delta. \tag{13}$$

Otherwise, it will be washed away by the plasma expansion. Close to the target surface, where $\lambda_D = \lambda_{D0}$, this can occur at $\omega_b t \geqslant 8\omega_p/\omega_b \approx 320$, i.e., late in the expansion process. In general, we find that an instability is likely to occur only far behind the ion expansion front, which is located where $L_\Delta = \lambda_D$ [23]. This means that ion-acoustic instabilities are not dangerous for the development of thermal emittance in the fastest ions.

IV. INTEGRATED SIMULATIONS OF ION ACCELERATION AND HEATING

In the following we present results from two integrated models that combine laser absorption, fast electron generation and transport, and finally heating and acceleration of ions. Our approach comprises a kinetic description of the plasma via the Vlasov equation using a particle-in-cell model, and includes a description of binary Coulomb collisions that will be described in the following.

A. Monte Carlo binary collision model

Both the one-dimensional particle-in-cell code LPIC-MC [29] and the two-dimensional code PICLS [30] include small-angle binary Coulomb collisions using Takizuka and Abe's (TA) model [31], modified to treat the collision particle kinetics relativistically correct [30]. That means that the momenta of any two collision partners are Lorentz-transformed between laboratory and center-of-mass (c.m.) frame, instead of using Galilei transforms as in TA. This is important for a correct description of energy transfer when electron velocities are close to light velocity, which is the case when the normalized laser amplitude $a=eE/m\omega c\approx 1$. The TA model is "fully collisional" in that it includes collisions between all combinations of species that are present in the plasma.

The principles of the binary collision operator are sketched here only briefly in the most simple case; for more details we refer to Refs. [31–34]. Collisions are executed in each time step between selected random partners in spatially localized regions that extend over a Debye screening length; these collision cells coincide with the PIC cells. Particles that are located in different cells do not interact. In a $Z=1$ plasma with an even number of electrons and protons in each cell, one first executes intraspecies collisions between particles number m and $m+1$ for electrons and protons, then interspecies collisions between electron number m and proton number m. In each binary collision process, the relative particle velocity $u=|\mathbf{u}|$ in the c.m. frame is determined and the collision frequency is calculated according to Spitzer's formula [35] (in cgs units)

$$\nu_{\alpha\beta}=\frac{4\pi^{3/2}q_\alpha^2 q_\beta^2 \ln\Lambda n_{\alpha\beta}}{m_{\alpha\beta}^2 u^3}, \tag{14}$$

where q_α represents the charge of particle α, $\ln\Lambda$ is the Coulomb logarithm which is assumed to be constant here, $n_{\alpha\beta}=\min(n_\alpha,n_\beta)$, and $m_{\alpha\beta}=m_\alpha m_\beta/(m_\alpha+m_\beta)$ is the reduced mass. The azimuthal scattering angle in the c.m. frame is determined from a Gaussian distribution with a width $\nu_{\alpha\beta}\Delta t$ that is generated from two uniform random number distributions via the Box-Muller method [36], while the poloidal scattering angle ϕ is directly determined from a uniform random number distribution between 0 and 2π. If $\nu_{\alpha\beta}\Delta t>0.5$, the small-angle scattering assumption of the TA model breaks down and the azimuthal scattering angle is determined from a uniform distribution on the sphere; to do this, $\cos\theta$ is determined from a uniform distribution of random numbers. The relative-velocity vector is rotated by these angles, then transformed back into the laboratory system and added to the scattering particle velocities. We have tested our implementation of the TA model successfully against analytic models for the temperature equilibration of a two-component plasma [33].

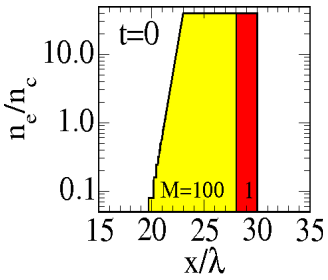

FIG. 6. (Color online) Initial target setup, i.e., ion density vs position. All ions except a thin layer on the rear surface—as indicated in the figure—have an artificially large mass.

B. 1D simulation results

As a first step we want to study the generation of a purely *thermal* emittance in the idealized scenario of a single beamlet of ions, as described earlier in Sec. I; the transverse structure of electron transport in the target will be considered separately. In order to study energy transfer between electrons and ions including the full dynamics of the plasma expansion and collisional heating, we have set up a one-dimensional collisional particle-in-cell Monte Carlo (PIC-MC) simulation of a short pulse laser interacting with a foil. In the simulation the laser pulse has an intensity $I_L=10^{19}$ W/cm^2 at 1 μm wavelength. The setup for the simulation is shown in Fig. 6. The target is modeled as a proton-electron plasma at $40n_c$ density, where $n_c=10^{21}$ cm^{-3} is the critical density, and a thickness of 8λ. It consists of an exponential density ramp with a thickness of 3 μm and a gradient length of 2 μm. Our simulation box has a total size of 110 μm. In order to suppress ion acceleration from the front which might interfere with ions launched from the rear target surface, we have artificially set the ion mass to $100m_p$ at the front of the target; we have verified that this has only little effect on absorption, electron transport, and thereby on ion acceleration off the rear surface, but it suppresses the acceleration of protons from the front and their interference with ion acceleration off the rear surface. The numerical resolution of our simulation is 1500 cells per micrometer, consistent with the Debye length at a temperature of 300 eV. The initial electron temperature is set to 1 keV, so that numerical heating plays no significant role over the time span of our simulation, while the target is not yet expanding by itself on the time scale of the laser interaction. Each cell contains 1000 electrons and ions in order to have good statistics for the analysis of the ion temperature in dilute parts of the beam. The value of the Coulomb logarithm in the collision model is fixed to $\ln\Lambda=5$ for simplicity. In both the collisional and the collisionless simulations, we find the electron temperature to be approximately 1 MeV, consistent with the usual scaling for $\mathbf{j}\times\mathbf{B}$ heating [37].

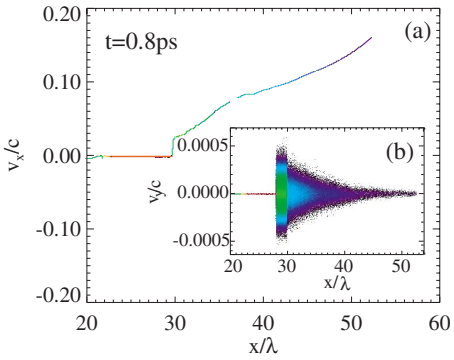

FIG. 7. (Color online) Ion phase space in PIC simulation at 0.8 ps. Color scales represent phase space density: Darker tones correspond to lower densities. (a) Longitudinal; (b) transverse.

Figure 7 gives transverse and longitudinal ion phase space at time 0.8 ps after the laser interaction. Colors refer to phase space density: Darker colors correspond to lower density. The narrow phase space of the ions at $x < 28\lambda$ belongs to the artificially heavy ions that remain relatively cold during the laser interaction. The cone shape of the ion phase space behind the target in Fig. 7(a) is caused by the fact that those protons that are accelerated last experience the most collisional heating in the dense plasma, while the fastest ions are accelerated before substantial heating sets in.

Figure 8 combines longitudinal and transverse phase space information in giving the beam transverse temperature as a function of proton kinetic energy, as read off Fig. 7. It is the centerpiece of this work, because it correlates the local transverse beam temperature of the protons with their longitudinal kinetic energy. We will relate this information to the experimental results we presented in Fig. 2 in the discussion in Sec. IV E below. The reason why we chose the beam temperature, and not the emittance, as a parameter for comparison with the experiment, is that the temperature is independent of the source size. This allows us to compare the

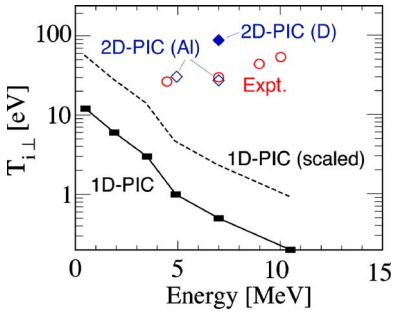

FIG. 8. (Color online) Transverse beam temperature plotted vs longitudinal kinetic energy for experiment, 1D PIC, and 2D PIC, simulations. Connected rectangles refer to 1D PIC simulation result (using $T_{c,0}=1$ keV) and open circles to experimental results described in Sec. IV E. The broken line represents the 1D simulation result after scaling by factor $\sqrt{20}$, corresponding to $T_{c,0}=50$ eV (see Sec. III A). 2D PIC results are shown for both the reference $Z=1$ target (D) (filled diamond) and the Al target with $Z=13$ (open diamonds). The 2D PIC results are computed from a least-rms fit to the set of particles shown in Fig. 10.

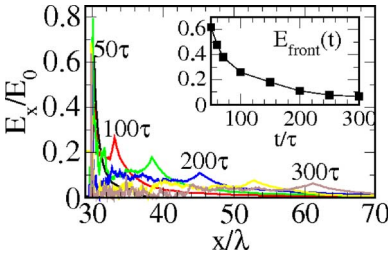

FIG. 9. (Color online) (a) Snapshots of longitudinal electric field behind target at four times, in units of the laser cycle τ. (b) Maximum value of the electric field as marked in plot (a) vs time.

experimental results, and eventually 2D simulations presented below, with 1D results.

Figure 9 shows snapshots of the longitudinal electric field, given in units of the laser electric field $E_0=\omega_L m_e c/e$. Here ω_L is the laser frequency. The numerical value of E_0 for $\lambda_L=1$ μm is roughly 3.2×10^{12} V/m. Note that the maximum of the electric field coincides with the ion expansion front [11].

We have performed an additional simulation with no collisions that is not shown here. This fiducial run confirms that there is no numerical heating in the transverse direction. Instead, we observe transverse oscillations in the velocity of the fastest expanding protons at an amplitude of $10^{-5}c$, which at time $\approx$0.8 ps is approximately 10$\times$ smaller than in the comparable collisional simulation. These oscillations can be explained as a consequence of the numerically generated radiation, as explained below. They can also be observed in the collisional simulation, but here they become visible only at later times. A further result of the fiducial simulation is that the evolution of the longitudinal electric field behind the target is hardly affected by the collisionality of the simulation under the present conditions [34].

C. 2D simulation results

We will now turn to two-dimensional fully collisional simulations, resolving essential features of the laser-generated electron beam's transverse structure. The physical parameters are identical to the one-dimensional setup described in Sec. IV B; the transverse target size is 64 μm. The resolution is 25 cells per μm and 200 particles per cell. Numerical heating is avoided by using a fourth-order interpolation scheme.

Figure 10 shows the transverse phase space of the proton beam from which the beam temperatures in Fig. 8 are determined. Figure 10(a) contains the complete phase space of select protons with three longitudinal kinetic energies between 5 and 10 MeV. The maximum divergence for 5 MeV protons is 0.15 rad corresponding to an angle of 10° in agreement with Fig. 2 of Ref. [3]. For a comparison with the experiment, where temperature was determined from the central grove alone thus eliminating the influence of the laser intensity profile, we magnify the central region of Fig. 10(a). Dashed ellipsoids in Fig. 10(b) indicate the area enclosed by the particles. The small ellipse is representative of the irreducible 2D emittance; the large one contains contributions

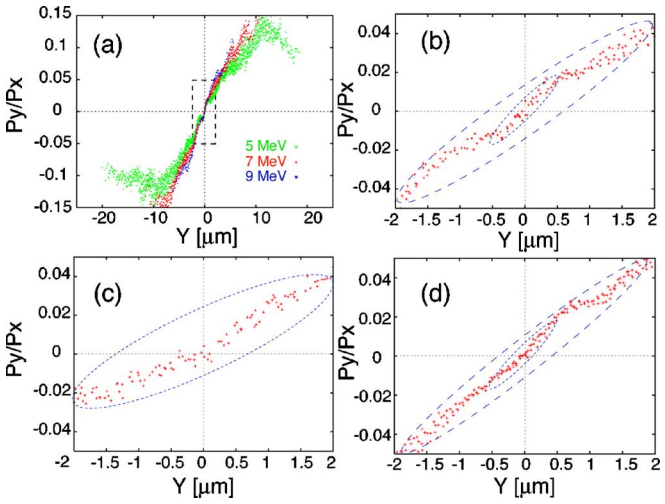

FIG. 10. (Color online) Transverse proton phase space in 2D simulation at time 800 fs, showing $p_y' \equiv p_y/p_z$, where y is the laser polarization direction; (a) full phase space; (b) blowup of the region indicated in (a); (c) same as (b), but from collisionless fiducial run; (d) same as (b) but with Al^{13+} in bulk target. The curves shown are not the phase-space ellipses, but rather denote the range of points included for the emittance calculations, as described in the text.

from μm-size structures on the target surface. Both are affected by the magnetic field on the rear target surface, which is generated by filaments shown in Fig. 11; the outer lobes at ±10° in Fig. 10(a) are caused by the lateral modulation of the sheath field which is due to the finite laser spot size. Figure 10(c) shows the result of a fiducial run without collisions (i.e., with the MC collision package switched off). One can clearly see how the beam quality is *reduced* in this case. In

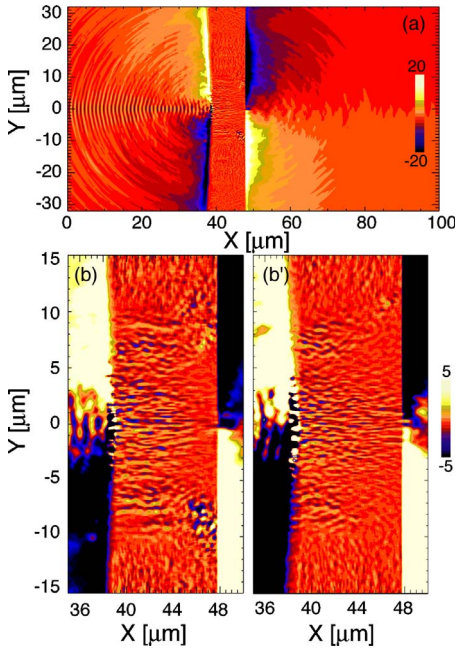

FIG. 11. (Color online) Azimuthal magnetic field component in 2D simulation at time 400 fs in units of MG; (a) global view of the reference case; (b) closeup of reference case; (b′) collisionless fiducial run.

an additional 2D simulation the bulk plasma was replaced by fully ionized Al^{+13} ions to enhance the effect of collisions in the bulk plasma. In order to have comparable conditions on laser absorption and particle acceleration, the preplasma and 1 μm layers at the front and the rear surface are identical with the previous simulations. The result for the transverse proton beam phase space is shown in Fig. 10(d). The corresponding emittance value is smaller than the one resulting from a pure proton target.

The underlying picture of the temporal evolution of the phase space is that, under ideal conditions, phase space starts out as a horizontally flat line of points corresponding to particles on the rear surface of the laser-irradiated target. After the protons lift off the surface, the correlation between initial position of particles and their directionality due to the envelope of the sheath field is represented by a finite slope of the lines in $y-p_y'$ phase space, while the finite width of the phase space ellipsoid is caused by (i) geometrical effects, e.g., structured surfaces (not included), (ii) thermal effects, as discussed above, or (iii) scattering of particles in EM fields near the surface. After the initial acceleration stage the beam spreads longitudinally and transversely as the protons follow their trajectories on the way to the detector. During this stage the phase space ellipse is sheared horizontally while its width shrinks, corresponding to an adiabatic cooling of the beam. This small effect is neglected in our analysis.

Figure 11 shows the azimuthal time-averaged magnetic field around the target at time 400 fs, both for the reference case with collisions, and a fiducial run without collisions. The larger magnetic field in the kinetic case demonstrates the role of the collisions in smoothing out the electron transport. The global view in Fig. 11 shows how the magnetic field drops from ±20 MG behind the target to almost zero at the front of the sheath at $x \approx 80$ μm.

The variations in the density of points in transverse phase space in Fig. 10 correspond to deflected protons from the inner (i.e., smaller radius) regions by the Lorentz force; also see the polarity of B_θ at corresponding locations in Fig. 11. While the structure inside the smaller ellipse is caused by spatiotemporal fluctuations of the EM field behind the target, the structure inside the larger ellipse is determined by beam filaments reaching the rear target surface. As their number is reduced by collisions, see Figs. 11(b) and 11(c), the phase space area is reduced as well. The comparison between the reference case and the collision-less fiducial run in Fig. 11 demonstrates that the structure of the magnetic field depends on the collisionality of the target due to the modified growth rate of transverse beam filamentation instability [38]. Note that also target thickness and laser intensity play an important role for the appearance of filaments at the rear target surface and therefore the quality of the proton images. Detailed studies of the latter effect are underway.

The two-dimensional (2D) transverse beam emittance is determined from Fig. 10 by considering the $y-p_y'$ phase space of protons with a given ±0.5 MeV range in longitudinal kinetic energies. Here y stands for the laser polarization direction, while x is the longitudinal coordinate and $p_y' = p_y/p_x$. The normalized rms emittance ϵ_N is given by the area that encloses all protons in phase space divided by π [3]. It is, however, difficult to compare the emittance to the

experimental one because it relies on target parameters not accessible in the 2D simulation, e.g., a thicker target. A better quantity to compare is the irreducible transverse beam temperature. It is independent of the source area on the target, so that a sensible comparison with the experiment, like in Fig. 8, or between experiments with different laser conditions is possible. The transverse beam temperature is determined from the rms width of the protons distribution inside the smaller phase space ellipse in Fig. 10(b) after subtracting a least-square fitted straight line. The resulting value for the 7 MeV protons is $\approx$70 eV.

D. Statistical noise and radiation in collisional particle simulations

Due to the small transverse particle velocities we consider, it is necessary to ensure that statistical fluctuations do not exceed physical effects. Note that the transverse ion velocities are approximately three orders of magnitude smaller than the longitudinal ones as shown in Fig. 7. In the scope of our present work we have to assume that the transverse motion of particles is caused either by collisions, or by electric and magnetic fields. We do not consider geometric effects, such as the longitudinal oscillation of a curved surface that would cause transverse modes of the electromagnetic field and result in a corresponding transverse particle motion [20].

It is an established fact that a finite layer of plasma will radiate transverse electromagnetic modes due to purely numerical effects in PIC simulations [39]. In the following, we will briefly explain the origin of these modes, and discuss their spectrum and their effect on particle dynamics in an expanding plasma. Let us start by considering the radiation emitted by a single plane macroparticle of density $\hat{n}$ that initially moves with a transverse velocity v_{y0} and represents a current $j_{y0}=\hat{q}\hat{n}v_{y0}$. There will be an initial electric displacement

$$E_{y0} = -\pi \Delta t j_{0y} \tag{15}$$

in the cell where the particle is located. Then transverse electric and magnetic fields and current will evolve according to Maxwell's equations on the grid

$$\frac{\partial j_y}{\partial t} = 2\pi \hat{n} E_y, \tag{16}$$

$$\frac{\partial E_y}{\partial t} = -2\pi j_y - \frac{\partial B_z}{\partial x}, \tag{17}$$

$$\frac{\partial B_z}{\partial t} = -\frac{\partial E_y}{\partial x}. \tag{18}$$

Poisson's equation is omitted here since in a purely transverse motion there is no charge separation in 1D. Assuming that the macroparticle is located at point $x=0$ at all times, and neglecting the electric displacement at times $t>0$, we can solve these equations for $x>0$ by ansatz

$$E_y(x,t) = E_{y0}\Theta(t-x)\exp[kx - \omega t], \tag{19}$$

$$j_y(x,t) = j_{y0}\delta(x)\exp[-\omega t], \tag{20}$$

where $k=\omega$ and $\omega=2\pi^2\hat{n}\Delta t$. Observed at a fixed point, the electric field decays exponentially in time. The corresponding spectrum of the emitted radiation is going to be

$$E_\omega \propto 1/(1+\omega), \tag{21}$$

as can be confirmed in simple setup with a single particle in a box. The emitted radiation spectrum is similar in a scenario of a collisionless plasma slab with a thickness $d \gg l_s$ large compared to the plasma skin depth $l_s=c/\omega_p$ [26]. Even when the transverse current is set to zero intially, for example by carefully initializing the particles with pairwise opposite velocity components (quiet setup), numerical fluctuations will eventually generate a transverse current that will have similar characteristics as discussed above. Analogously, binary collisions between particles act to randomize the particle motion and transfer energy from transverse into longitudinal degrees of freedom. In this respect, accounting for collisions between macro-particles makes the noise radiation emitted by a kinetic simulation resemble the single particle spectrum discussed in Eq. (21).

Knowing the spectrum of the radiation emitted by a plasma layer, by whatever mechanism, we are able to predict the corresponding particle motion. Due to the conservation of the canonic momentum, $(\mathbf{A}-q\mathbf{p})$, where $\mathbf{A}$ is the vector field potential, $\mathbf{p}$ is the kinetic particle momentum, and q is the particle charge, an oscillation in the transverse electric field will transfer momentum to particles that move in that field. And due to $\mathbf{E}=\partial\mathbf{A}/\partial t$, which transforms to $\mathbf{A}_\omega=\mathbf{E}_\omega/\omega$ in frequency space, the vector field potential will preferably pick up low-frequency modes of the electric field. This leads to a pickup of small-amplitude transverse oscillations of the ions in collisional PIC simulations of expanding hot plasma, as observed in collisional, but also in collisionless simulations at late times. The field amplitude that is emitted numerically from a plasma layer similar to the ones discussed here is of the order $10^{-4}E_0$, resulting in an intensity roughly eight orders of magnitude below that of the laser radiation.

Finally, we want to comment briefly on the importance of physical radiation losses from a plasma. A simple estimate shows that they play only an insignificant role in the scenarios and on the time scales we consider here. While bremsstrahlung is not included in a kinetic description, the total bremsstrahlung radiative loss rate [40]

$$J = 1.4\times 10^{-29} Z^2 T_{\mathrm{eV}}^{1/2} N_+ N_e \ \mathrm{erg\ cm^{-3}\ s^{-1}}, \tag{22}$$

where Z is the effective ion charge state, T_{eV} the electron temperature in eV, while N_{+e} are ion and electron densities. For the parameters used in our studies above with $N_e=N_+=40n_c$, $Z=1$, and $T=50$ eV, we get a loss rate $J\approx 0.8\times 10^{16}$ W/cm^3 yielding 4×10^{12} W/cm^2 for a 5 μm thick layer of optically thin plasma. The corresponding energy spectrum of the emitted radiation is proportional to $\exp[-\nu/\nu_0]$, in contrast to our simulations where we get a spectrum $\propto\nu^{-1}$. Similarly, inverse Thomson scattering and radiation damping are not included in a PIC description, and they play a role only for radiation intensities beyond the scope of this work.

E. Discussion

Comparing our one- and two-dimensional simulations with collisions allows us to separate purely thermal from geometrical effects, i.e., those which are due to the filamentation of the electron beam in the target. We find that the majority of the final emittance is due to scattering of protons in azimuthal magnetic fields that are connected to current filaments exiting the target.

Let us first address the purely thermal emittance. Using the information given in Fig. 8, we can compare our 1D simulation results for the transverse beam temperature to the experimental results for the transverse emittance discussed in Sec. II and in Ref. [3]. We now discuss briefly our choice of the initial electron temperature $T_c(0)$. In the simulation presented above $T_c(0)$ is determined by the technical requirement to resolve the electron Debye length, in order to avoid numerical heating while keeping the resolution low enough to still be able to handle the problem size [39]. Note that the value of $T_i \approx 0.3$ eV for the fastest protons found in our simulation agrees with the value found in the temporal history of T_i at 10 fs found in the simple equilibration model, compare Fig. 3(a). While our choice of $T_c(0)$ cannot be justified by direct observation, it is important to understand the sensitivity of the final result (i.e., ion heating) to this parameter. The result, as shown in Fig. 3(b), is that varying the initial value of $T_c(0)$ between 1 eV and 1 keV makes only a factor of 4 difference in the final value of the ion temperature at the time of liftoff (i.e., 10 fs). This makes our final result rather insensitive to the choice of initial conditions, given other assumptions and unknowns about the laser interaction that make a one-to-one mapping with the experiment difficult. In particular, using Fig. 3(b), one can scale the simulation results for $T_{c,0}=1$ keV to obtain the transverse ion temperatures for an assumed value $T_{c,0}=50$ eV as discussed earlier. The result is also presented in Fig. 8 as the broken line.

As shown in Fig. 8 the experimental values for the transverse beam temperature are more than one order of magnitude larger than those found in our 1D simulation, even when accounting for more realistic target conditions like higher ion charge states or different values of the initial cold electron temperature estimates. This suggests that the upper limits on the emittance found in the experiment are not affected by thermal effects. An important assumption of the phase space snapshot presented in Fig. 7 is that the acceleration is essentially finished at 0.8 ps. This is confirmed by a comparison with Fig. 9, which shows that at this time the electric field at the front has dropped to roughly 15% of its maximum value at the beginning of the expansion. Note that this time scale also motivates our choice of the final time in Fig. 3, since it presents an upper limit for how long midenergy ions remain in the target. The same is true for the 2D simulation presented in Figs. 10 and 11.

From our 2D simulations we conclude that the majority of the observed proton beam emittance for the cases presented here is generated by fluctuating azimuthal magnetic fields next to the rear target surface, which are directly caused by the filamented electron beam; the magnetic fields scatter protons as they are accelerated in the electrostatic sheath field [41]. The bulk target resistivity, on the other hand, makes the electron beam more smooth and can thereby reduce the proton beam emittance. This view is confirmed by our results with no collisions, where the beam quality is worse, and those with stronger collisions in the bulk, where the result is smaller proton beam emittance; compare Fig. 8. The collisional mean-free path of an MeV electron in our reference target is ≈ 50 cm, while it is ≈ 0.3 cm in the $Z=13$ case [26]. Since this is much larger than the total target thickness in our simulation, the smoothing effect of the bulk is small; however, once it is replaced by high-Z materials at realistic densities, e.g., Cu, we expect a stronger scattering of the electron beam in the target. While this remains to be investigated by future simulations, recent experiments have already found the quality of proton beams off gold targets to be much better than that off Copper targets, confirming the role of collisions in the bulk [14]. We expect little difference between our present 2D results and comparable 3D runs because of similar magnitudes of the electric and magnetic field strengths in filaments [42].

Hence we need to distinguish between the "irreducible" 2D emittance, indicated by the inner ellipse in Fig. 10(b), on the one hand, related to fast fluctuations of the electromagnetic fields behind the target even without filaments. On the other hand, the "nominal" emittance as indicated by the outer ellipse is determined by the presence of filaments. Both values depend on the particular conditions, i.e., laser intensity, target thickness, and the free-electron density Z_{eff}, in the bulk target. The deflection of protons in the magnetic field behind the target can become strong enough as to form structures on the RCF images. In Fig. 8 we present only the irreducible contribution; the nominal one is approximately four times larger. A direct comparison with the experiment is difficult because both the effective charge state (i.e., material) and the target thickness were larger in the experiment than in our 2D simulation. Since this leads to potentially underestimating the smoothing of the electron beam in the bulk target, our results in Fig. 8 overestimate the beam temperature; the experimental results, on the other hand, overestimate the beam temperature because of the systematic combination of geometric and irreducible effects. Note that, although the real phase space volume occupied by the particles in Fig. 10 is smaller than that of the ellipses, the latter characterize the "useful" phase space volume, independent of the application.

V. CONCLUSION

We have studied the origin of the transverse emittance in short-pulse laser-accelerated ion beams by means of analytic tools and numerical one- and two-dimensional collisional PIC simulations. Our central result is that the dominating mechanism responsible for the beam emittance is the filamentation of the electron beam near the front surface of the dense target; this contributes about 90% of the emittance measured in Ref. [3], but can be reduced by enhancing the resistivity of the bulk material. The second most important contribution comes from electron-ion collisions before the ions are accelerated. An important conclusion with respect to future target design is that electron-ion collisions in the

dense bulk target act to smooth out the filamentary structure of the hot electron beam and thereby *reduce* the irreducible 2D emittance, while at the same time they have no large effect on the thermal emittance. This explains the superior imaging quality of proton beams accelerated off high-Z targets, as compared to low-Z or plastic targets by their inherently higher resistivity [14]. The target thickness should be subject to an optimization in future studies, since thicker targets will cause the electron beam to spread out wider, reducing the accelerating electric field behind the target and therefore the maximum kinetic energy of the ions, while thin targets provide inferior beam smoothing or even allow shock breakthrough [43], therefore reducing the beam quality.

ACKNOWLEDGMENTS

This work was supported in part by DOE/NNSA under UNR Grant No. DE-FC52-01NV14050 and Grant No. DFG-KE866, Deutsche Forschungsgemeinschaft. This work was performed under the auspices of the U.S. Department of Energy by University of California Lawrence Livermore National Laboratory under Contract No. W-7405-ENG-48.

[1] W. P. Leemans *et al.*, Nature Phys. **2**, 696 (2006).
[2] M. Borghesi *et al.*, Fusion Sci. Technol. **49**, 412 (2006).
[3] T. E. Cowan *et al.*, Phys. Rev. Lett. **92**, 204801 (2004).
[4] S. Humphries, *Charged Particle Beams* (Wiley-Interscience, New York, 1990).
[5] T. Toncian *et al.*, Science **312**, 410 (2006).
[6] R. A. Snavely *et al.*, Phys. Rev. Lett. **85**, 2945 (2000).
[7] M. Roth *et al.*, Phys. Rev. Lett. **86**, 436 (2001).
[8] P. Patel *et al.*, Phys. Rev. Lett. **91**, 125004 (2003).
[9] A. Boyer *et al.*, Phys. Today **55**, 34 (2002).
[10] M. Borghesi *et al.*, Phys. Rev. Lett. **88**, 135002 (2002).
[11] L. Romagnani *et al.*, Phys. Rev. Lett. **95**, 195001 (2005).
[12] J. Lawson, *The Physics of Charged Particle Beams* (Clarendon Press, Oxford, 1988).
[13] J. Fuchs *et al.*, Phys. Rev. Lett. **94**, 045004 (2005).
[14] J. Fuchs *et al.*, Phys. Rev. Lett. **91**, 255002 (2003).
[15] M. Manclossi, J. J. Santos, D. Batani, J. Faure, A. Debayle, V. T. Tikhonchuk, and V. Malka, Phys. Rev. Lett. **96**, 125002 (2006).
[16] A. Kemp and H. Ruhl, Phys. Plasmas **12**, 033105 (2005).
[17] M. Hegelich *et al.*, Phys. Plasmas **12**, 056314 (2005).
[18] T. E. Cowan *et al.*, in *High Brightness Beams* (World Scientific Press, Singapore, 2000).
[19] M. Borghesi, A. J. Mackinnon, D. H. Campbell, D. G. Hicks, S. Kar, P. K. Patel, D. Price, L. Romagnani, A. Schiavi, and O. Willi, Phys. Rev. Lett. **92**, 055003 (2004).
[20] H. Ruhl, T. E. Cowan, and J. Fuchs, Phys. Plasmas **11**, L17 (2004).
[21] N. Klassen *et al.*, Med. Phys. **24**, 1924 (1997).
[22] L. Reinstein *et al.*, Med. Phys. **24**, 1935 (1997).
[23] P. Mora, Phys. Rev. Lett. **90**, 185002 (2003).
[24] Y. Sentoku, T. E. Cowan, A. Kemp, and H. Ruhl, Phys. Plasmas **10**, 2009 (2003).
[25] S. Gitomer *et al.*, Phys. Fluids **29**, 2679 (1986).
[26] D. Book, NRL Plasma Formulary, Washington, DC, 1990.
[27] R. Kodama *et al.*, Nature (London) **418**, 933 (2002);E. Martinolli *et al.*, Phys. Rev. E **73**, 046402 (2006).
[28] V. Sotnikov *et al.*, J. Geophys. Res. **99**, 23473 (1994), and articles cited therein.
[29] R. Pfund, R. Lichters, and J. Meyer-ter-Vehn, in *Superstrong Fields in Plasmas*, edited by M. Lontano *et al.*, AIP Conf. Proc. No. 426 (AIP, New York, 1998), p. 141.
[30] Y. Sentoku *et al.*, J. Phys. Soc. Jpn. **67**, 4084 (1998).
[31] T. Takizuka and H. Abe, J. Comput. Phys. **25**, 205 (1977).
[32] R. Shanny, J. Dawson, and J. Greene, Phys. Fluids **10**, 1281 (1967).
[33] R. Pfund, Ph.D. thesis, TU München, 1999.
[34] A. Kemp, R. Pfund, and J. Meyer-ter-Vehn, Phys. Plasmas **11**, 5648 (2004).
[35] L. Spitzer and R. Härm, Phys. Rev. **89**, 977 (1953).
[36] *Numerical Recipes in C++*, 2nd ed., edited by W. Press *et al.*, (Cambridge University Press, Cambridge, UK, 2002).
[37] S. C. Wilks, W. L. Kruer, M. Tabak, and A. B. Langdon, Phys. Rev. Lett. **69**, 1383 (1992).
[38] Y. Sentoku *et al.*, Phys. Plasmas **7**, 689 (2000).
[39] C. Birdsall and A. Langdon, *Plasma Physics via Computer Simulation* (Adam Hilger, New York, 1991).
[40] Y. Zel'dovich and Y. Raizer, *Physics of Shock Waves and High Temperature Hydrodynamic Phenomena* (Academic Press, New York, 1967).
[41] Y. Murakami *et al.*, Phys. Plasmas **8**, 4138 (2001).
[42] J. C. Adam, A. Heron, and G. Laval, Phys. Rev. Lett. **97**, 205006 (2006).
[43] M. Kaluza, J. Schreiber, M. I. K. Santala, G. D. Tsakiris, K. Eidmann, J. Meyer-ter-Vehn, and K. J. Witte, Phys. Rev. Lett. **93**, 045003 (2004).